DACouplerNet: A Dual-Architecture Artificial Neural Network for IPT Magnetic Coupler Modeling with Reduced Data-Sampling Overhead

Zhicong Huang, *Senior Member, IEEE*, Jun Cheng, and Guozhen Hu

***Abstract*—Magnetic couplers are vital in inductive power transfer (IPT) systems, yet their parameter design often relies on time-consuming finite element method (FEM) and iterative optimization. An accurate and efficient model is therefore essential to guide the design process. Analytical methods can only describe magnetic couplers without ferrite cores or with regular geometries, and their numerous simplifications limit calculation accuracy for complex designs. While FEM offers higher precision, it requires extensive computational resources and is inefficient for iterative design. Our previously developed neural network based magnetic coupler model can help to accelerate the design process, but still incurs a significant data-sampling overhead issue due to exhaustive data sampling and labeling. To address these challenges, this paper proposes a dual-architecture artificial neural network for IPT magnetic coupler modeling (DACouplerNet) designed to substantially reduce data-sampling overhead. By leveraging the physical insight that the dominant effects of the input variables (i.e., the geometric parameters and offset/core parameters) on the outputs (i.e., the self- and mutual inductances) can be approximately decoupled within the investigated parameter ranges, the proposed DACouplerNet employs two subnetworks to separately model the geometric effects and offset/core effects. The final prediction is obtained by aggregating the outputs of both subnetworks. As a result, the model can be effectively trained using only 0.2% in terms of samples for training over the full investigated parameter-combination space, thereby reducing the reliance on exhaustive FEM-based data sampling in traditional IPT magnetic coupler modeling.**

***Index Terms*—Inductive Power Transfer, Magnetic Coupler, Artificial Neural Network, Reduced data-sampling Overhead.**

I. Introduction

INDUCTIVE Power Transfer (IPT) technology has garnered significant attention in recent years due to its advantages of eliminating traditional cable constraints, enhancing system safety, and reducing maintenance costs [1], [2]. Moreover, it has broad application prospects in scenarios such as electric vehicles, consumer electronics, implantable medical devices, and underwater robots [3]–[7]. IPT operates on the principle of electromagnetic induction, enabling efficient energy transfer via magnetic coupling between transmitter and receiver coils [8]. As the core structural component of IPT systems, coil parameters such as self-inductance (L) and mutual-inductance (M) directly affect power transfer efficiency and system stability. Therefore, accurate and efficient coil parameter modeling is essential for system design [9], [10].

Traditional coupler modeling approaches primarily rely on analytical methods. While these methods provide clear physical insights, their idealized assumptions, such as infinite magnetic cores [14], [15] or perfect alignment [12], limit practical applicability.

Consequently, analytical models often exhibit low prediction accuracy and involve cumbersome mathematical derivations [11]–[16]. For example, Ref. [12] proposed an accurate calculation method for high-frequency planar magnetics but overlooked coil misalignment effects, while Ref. [13] incorporated misalignment but neglected magnetic core impacts. Many studies approximate magnetic cores as infinite planes using the multiple mirroring method [14], [15], an assumption that severely limits engineering applicability. Numerical approaches such as the finite element method (FEM) have been introduced to overcome these accuracy limitations by discretizing the electromagnetic field domain, yielding more precise and versatile results [17]–[19]. However, FEM-based optimization remains computationally expensive, particularly in multi-parameter iterative design. Ref. [17] did not fully explore the design space during parameter scanning, whereas Refs. [18], [19] reported prohibitively long computation times for coil optimization. These trade-offs between the interpretability of analytical approaches and the computational burden of FEM motivate the development of data-driven modeling techniques for IPT magnetic couplers.

In recent years, machine learning has been increasingly applied to the modeling and optimization of IPT magnetic couplers. For example, Ref. [20] proposed a machine learning based method for accurately estimating the Q-factor of couplers. Ref. [22] combined neural networks with multi-objective optimization for data-driven coil design, yet sparse sampling limited the model's ability to capture complex nonlinear relationships, thereby reducing its generalization capability. In Ref. [23], a systematic optimization framework integrating circuit, electromagnetic, and thermal models was developed

Manuscript submitted 29 December 2025; revised 2 July 2026 and 20 August 2026; accepted 16 September 2026. This work was supported in part by the National Natural Science Foundation of China under Grant 52577198, in part by the Guangzhou Municipal Science and Technology Bureau under Grant 2025A04J7064, in part by the Fundamental Research Funds for the Central Universities, and in part by the Science and Technology Planning Project of Guangdong Province under Grant 2025A0505010015. (Corresponding author: Guozhen Hu)

Zhicong Huang and Juncheng are with the Shien-Ming Wu School of Intelligent Engineering, South China University of Technology, Guangzhou 510006, China. (e-mail: zhiconghuang@scut.edu.cn, wichengjun@mail.scut.edu.cn).

Guozhen Hu is with the School of Electrical and Electronics Engineering, HuBei Polytechnic University, Huangshi 435003, China. (e-mail: huguozhen@hbpu.edu.cn).

for loosely coupled PCB spiral coils. However, these studies [20]–[23] overlooked coil misalignment effects, which restrict their practical applicability. Ref. [24] further introduced a transfer learning-based inductance prediction method that enabled knowledge transfer between circular and rectangular coils. In our previous work [21], a machine-learning-based design framework employing stacked models was proposed, demonstrating that neural network surrogates can effectively replace FEM to accelerate iterative design. Nevertheless, all the aforementioned studies share a common limitation, i.e., the requirement for extensive labeled data. Typically, 80-90% of the full investigated space is used for training, and obtaining such a large number of labeled samples necessitates exhaustive FEM simulations. As the number of design variables increases, the cost of data generation grows prohibitively high. Therefore, existing machine learning approaches for IPT magnetic coupler modeling have not effectively addressed the data-sampling overhead problem, which remains a major bottleneck for practical deployment.

To reduce the data-sampling overhead, this paper proposes a dual-architecture artificial neural network for IPT magnetic coupler modeling (DACouplerNet). The objective of the proposed DACouplerNet is illustrated in Fig. 1. The paper first reveals that the input variables of the magnetic couplers can be divided into two categories (i.e., geometric parameters and offset/core parameters), whose effects on the outputs (i.e., self- and mutual inductances) can be approximately decoupled without significant correlation. Leveraging this physical insight, the proposed DACouplerNet consists of two subnetworks with different modeling targets. One models the relationship between geometric parameters and the outputs, while the other captures the effect of offset/core parameters. The final prediction is obtained by aggregating the outputs of both subnetworks. As a result, the model can be effectively trained using samples for training accounting for only 0.2% of the full investigated parameter-combination space, thereby eliminating the reliance on exhaustive data sampling and labeling common in traditional IPT magnetic coupler modeling. Moreover, DACouplerNet achieves high prediction accuracy, with average prediction errors of 4.99% for mutual inductance and 3.05% for self-inductance. It should be noted that the model construction and experimental validation in this work are mainly based on circular magnetic couplers. Nevertheless, the proposed dual-architecture modeling framework is not inherently restricted to circular coils. For other unipolar and bipolar coil designs, the framework can be extended by defining topology-specific geometric variables and re-verifying the approximate-decoupling assumption between the parameter groups.

The rest of this paper is organized as follows. Section II analyzes the influences of geometric parameters and offset/core parameters to the outputs of the magnetic coupler, and figures out their uncorrelated relationship and feasibility to decompose the magnetic coupler modeling into two separated tasks. Section III details the proposed DACouplerNet for IPT magnetic coupler modeling. Section IV validates the efficacy of the proposed method, and Section V concludes the paper.

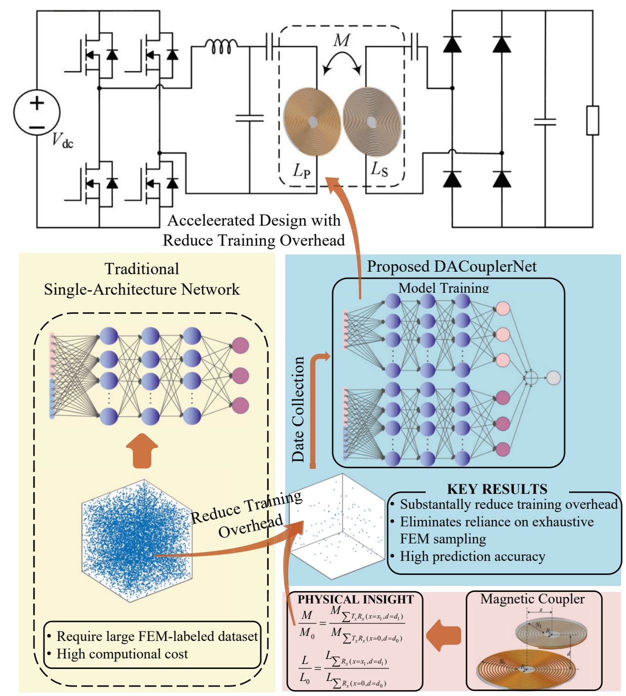

Fig. 1. Objective of the proposed DACouplerNet: reducing data-sampling overhead.

TABLE I
PARAMETER DEFINITION

Set	Parameter	Definition
X	a	Wire diameter
	R_w	Winding spacing
	N_1	Primary winding turns
	N_2	Secondary winding turns
	R_1	Primary inner diameter
	R_2	Secondary inner diameter
Y	h_1	Primary core thickness
	h_2	Secondary core thickness
	k_1	Primary core-to-coil outer diameter ratio
	k_2	Secondary core-to-coil outer diameter ratio
	d	Axial distance
	x	Lateral distance

II. Analysis of Approximate Decoupling between Geometric and Offset/Core Parameters

This section examines the approximately decoupled effects of two distinct groups of input parameters on the design outputs of magnetic couplers, namely the self-inductance and mutual inductance. The first group, which is denoted as X, indicates the geometric parameters and comprises the wire diameter a, winding spacing R_w, primary and secondary winding turns N_1 and N_2, and the primary and secondary inner diameters R_1 and R_2. The second group, denoted as Y, includes offset and magnetic core parameters, specifically the primary and secondary core thicknesses h_1 and h_2, the primary and secondary core-to-coil outer diameter ratios k_1 and k_2, the axial distance d, and the lateral distance x. The definitions of the two parameter groups, X and Y, are summarized in Table I.

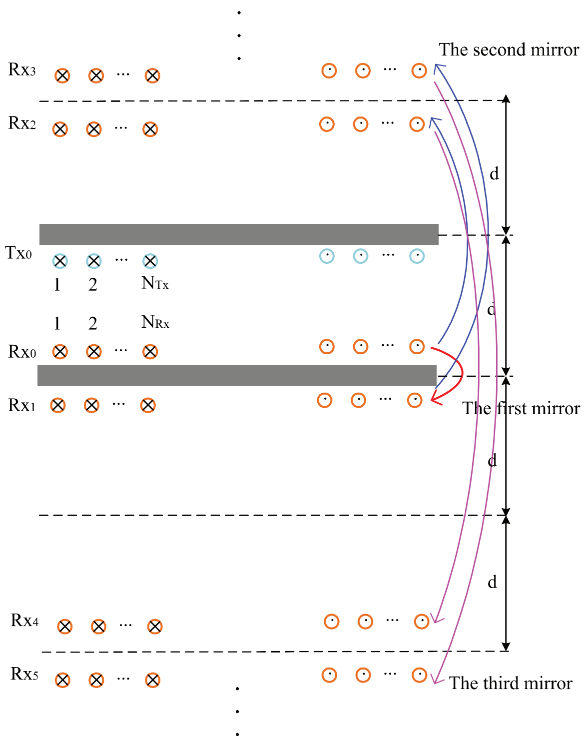

Fig. 2. Diagram of multiple mirroring method.

A. Analytical Calculation of Self- and Mutual Inductances of Magnetic couplers

Neumann's formula is a widely used method for calculating the self- and mutual inductances of magnetic couplers [16]. It expresses inductance as a line integral that captures the relative geometry and spatial arrangement of the conductors. Accordingly, the self- and mutual inductances of a single-turn coil can be given by

$$\begin{cases} M = \dfrac{\mu_0}{4\pi} \oint_{c_1} \oint_{c_2} \dfrac{1}{R}\, d\vec{l_1} \cdot d\vec{l_2}, \ \text{and} \\ L = \dfrac{\mu_0}{4\pi} \oint_{c_1} \oint_{c_1} \dfrac{d\mathbf{l}_1 \cdot d\mathbf{l}_2}{|\mathbf{r}_1 - \mathbf{r}_2|}. \end{cases} \tag{1}$$

For multi-turn coils, the inductance can be expressed as the superposition of the inductances between individual turns, given by

$$\begin{cases} M = \displaystyle\sum_{i=1}^{n_{T_x}} \sum_{j=1}^{n_{R_x}} M_{ij}, \ \text{and} \\ L = \displaystyle\sum_{i=1}^{n_{R_x}} \sum_{j=1}^{n_{R_x}} L_{ij}. \end{cases} \tag{2}$$

When the magnetic core thickness is limited, the multiple mirroring method can be used to account for the cross-coupling introduced by ferrite cores on both sides [14], [15]. As illustrated in Fig. 2, a conductor located between two parallel magnetic cores can be modeled by a finite set of dominant image currents that satisfy the magnetostatic boundary conditions at the core interfaces. Since higher-order images are progressively farther from the coil plane, their contributions decay rapidly and can be neglected. Accordingly, the mutual and self-inductances of the coupler in the presence of magnetic cores can be expressed in a unified form, given by

$$\begin{cases} M_{\sum T_x R_x} = \displaystyle\sum_{i=1}^{n} \left(M_{T_x R_{x_{2i-2}}} + M_{T_x R_{x_{2i-1}}} \right), \ \text{and} \\ L_{\sum R_x} = L_{R_x,\text{self}} + \displaystyle\sum_{i=1}^{n} M_{R_x R_{x_i}}, \end{cases} \tag{3}$$

n is the number of image iterations. $M_{T_x R_{x\ 2i-2}}$ and $M_{T_x R_{x\ 2i-1}}$ denote the mutual inductances between the transmitter coil Tx and the i-th pair of image receiver coils, respectively. $L_{R_x,self}$ is the intrinsic self-inductance of R_x without magnetic cores, and $M_{R_x R_{x\ i}}$ denotes the mutual inductance between the original coil and its i-th mirrored coil.

B. Approximate Decoupling Analysis of Geometric Parameters and Offset/Core Parameters

To numerically assess the approximately decoupled effects of geometric and offset parameters, this study examines the inductance ratios as functions of the relative positional offset. These ratios are derived as

$$\begin{cases} \dfrac{M}{M_0} = \dfrac{M_{\sum T_x R_x (x=x_1, d=d_1)}}{M_{\sum T_x R_x (x=0, d=d_0)}}, \ \text{and} \\ \dfrac{L}{L_0} = \dfrac{L_{\sum R_x (x=x_1, d=d_1)}}{L_{\sum R_x (x=0, d=d_0)}}, \end{cases} \tag{4}$$

where $(x = 0, d = d_0)$ denotes the initial position, and $(x = x_1, d = d_1)$ denotes the displaced position after a lateral offset and a change in axial distance.

A parametric study spanning the wire diameter a, turn spacing R_w, number of turns N_1 and N_2, and inner diameter R shows that coils with different dimensions exhibit consistent trends in M/M_0 and L/L_0 under the same offset, as shown in Fig. 3. This consistency further supports the decoupling between the geometric parameters and the offset parameters.

It is worth noting that the analytical model has two limitations:

1) Neumann's formula models the conductor as a filament, thereby neglecting the finite wire diameter.
2) The mirroring method approximates the magnetic core as an infinite plane, thereby ignoring finite core-size effects.

To address these limitations, FEM simulations are conducted. By accurately capturing the electromagnetic-field distribution and the core boundary conditions, the size-independent characteristics of M/M_0 and L/L_0 under offset conditions are further validated, as shown in Fig. 4.

As shown in Fig. 3 and Fig. 4, when the lateral offset is held constant, variations in the dimensional parameters have negligible impact on both the mutual-inductance ratio and the self-inductance ratio. Therefore, the effects of the dimensional parameters and the offset/core parameters on the inductances can be regarded as approximately decoupled within the investigated parameter ranges.

For Figs. 3 and 4, the core and offset-related parameters were fixed as $h_1 = h_2 = 2$ mm, $k_1 = k_2 = 1$, and $d = 30$ mm. In each subplot, one geometric parameter, i.e., a, R_w, N_1, N_2, R_1, or R_2, was varied independently,

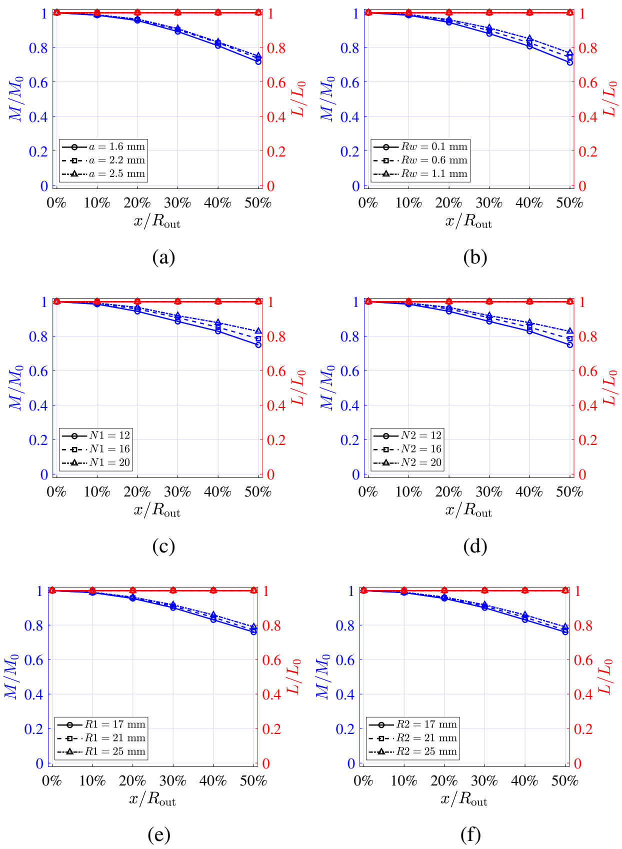

Fig. 3. Analytical calculation of the normalized inductance M/M_0 and L/L_0 of couplers with different structures varying with x/R_{out}.

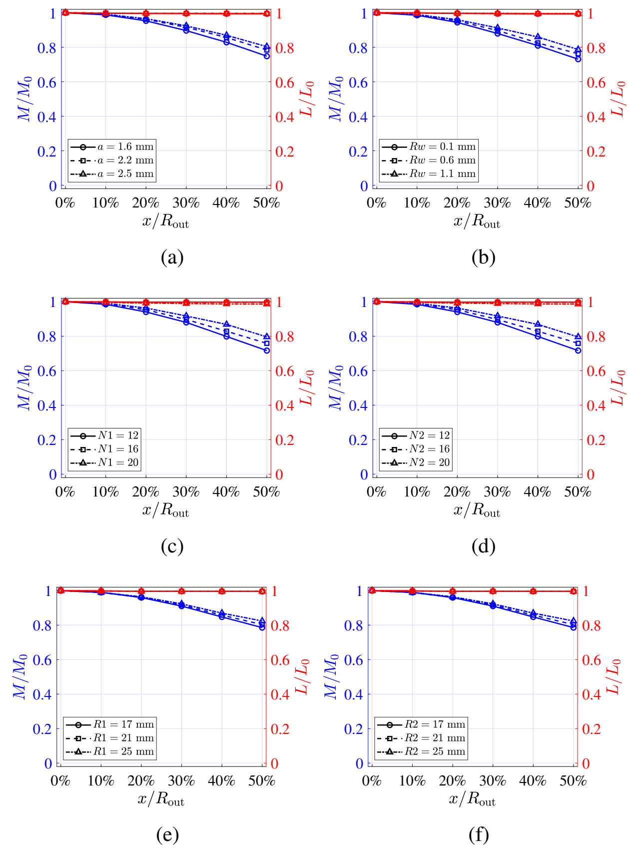

Fig. 4. Simulation calculation of the normalized inductance M/M_0 and L/L_0 of couplers with different structures varying with x/R_{out}.

while the remaining geometric parameters were kept at their nominal values. The normalized inductance ratios M/M_0 and L/L_0 were then calculated under different normalized lateral misalignments x/R_{out}.

Here, R_{out} denotes the average outer radius of the primary and secondary coils, and x/R_{out} is used to represent the normalized lateral misalignment.

Figs. 3 and 4 are used as representative examples to illustrate the normalized variation trends of M/M_0 and L/L_0 under different misalignment conditions, while Figs. 5 and 6 provide the overall linear and nonlinear correlation summaries between the two parameter groups.

To further substantiate the approximate decoupling between the two groups of input parameters, partial correlation analysis and Sobol second-order interaction analysis are introduced to evaluate the residual linear correlation and nonlinear interaction, respectively. The two groups of input parameters are denoted as X and Y, respectively, and the output variable is denoted as Z. By holding the variables in X constant, the correlation between Y and Z can be evaluated to quantify the residual correlation after removing the influence of X.

The corresponding partial correlation coefficient is given by

$$\rho_{YZ\cdot X} = \frac{\mathrm{Cov}(Y, Z \mid X)}{\sqrt{\mathrm{Var}(Y \mid X)\ \mathrm{Var}(Z \mid X)}}, \tag{5}$$

where $\rho_{YZ\cdot X}$ quantifies the degree of linear correlation between Y and Z after removing the influence of X.

Given (5) satisfies

$$\rho_{YZ\cdot X} = 0 \iff \mathrm{Cov}(Y, Z \mid X) = 0, \tag{6}$$

it indicates that, after controlling for X, no residual linear dependence exists between Y and Z. In practice, it is acceptable that when $|\rho_{YZ\cdot X}| < 0.05$, the influence of Y on Z can be regarded as negligible under the control of X. A similar interpretation applies when analyzing the influence of X on Z after controlling for Y.

The corresponding Sobol second-order interaction analysis coefficient is given by

$$S_{X,Y} = \frac{\mathrm{Var}_{X,Y}\left[\mathbb{E}(Z|X,Y) - \mathbb{E}(Z|X) - \mathbb{E}(Z|Y) + \mathbb{E}(Z)\right]}{\mathrm{Var}(Z)}. \tag{7}$$

$S_{X,Y}$ quantifies the fraction of the output variance contributed by the interaction between the geometric parameter group and the offset/core parameter group. There is no absolutely universal threshold for judging whether a second-order interaction can be neglected. For general engineering practice, if $S_{X,Y} < 0.05$, the interaction can be regarded as weak.

The partial correlation results are shown in Fig. 5. For both M/M_0 and L/L_0, the partial correlation coefficients remain small after controlling for the other parameter group, indicating weak residual linear correlation between X and Y.

The Sobol second-order interaction results are shown in Fig. 6. The interaction contribution between X and Y remains

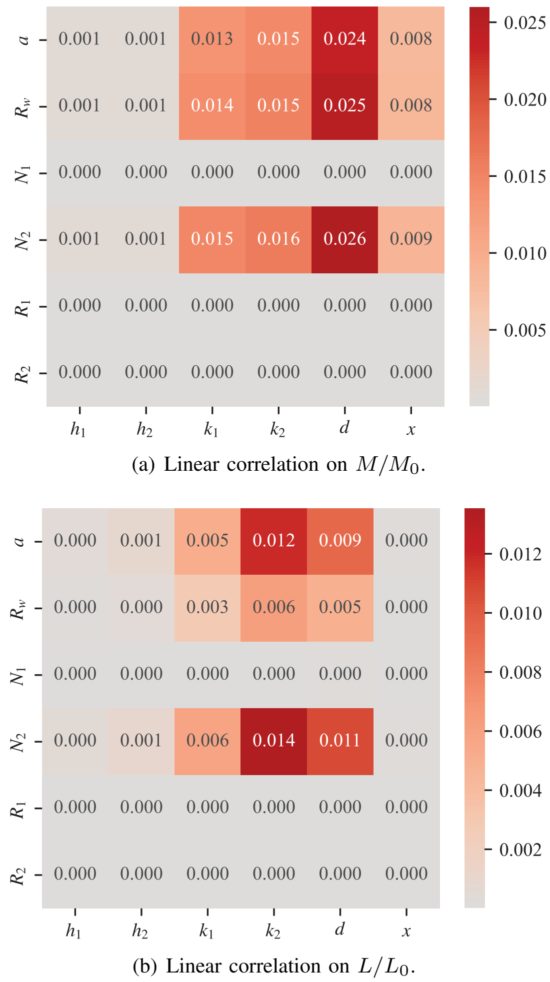

Fig. 5. Partial correlation influence of the geometric parameter group and the offset/core parameter group on the normalized outputs: (a) M/M_0 and (b) L/L_0.

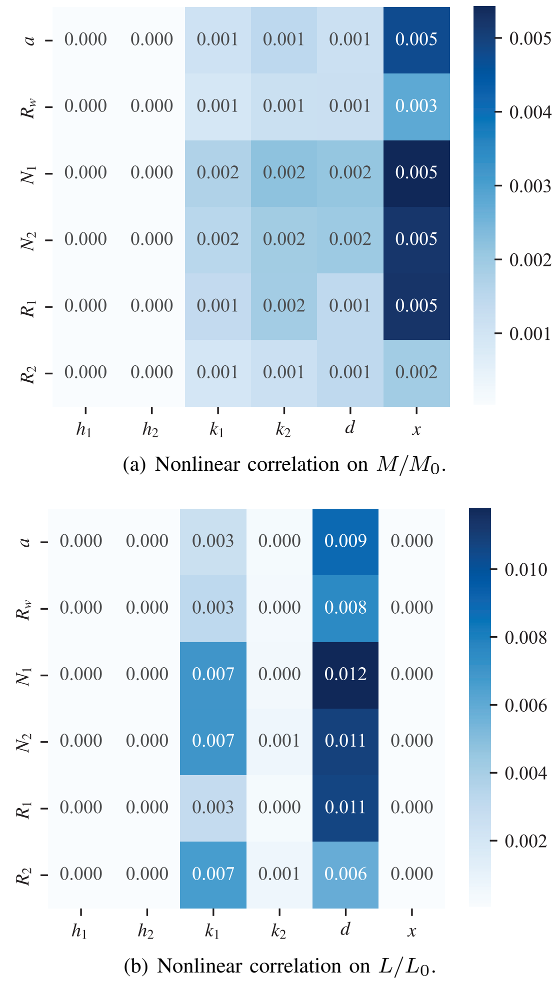

Fig. 6. Sobol second-order interaction analysis of the geometric parameter group and the offset/core parameter group on the normalized outputs: (a) M/M_0 and (b) L/L_0.

limited within the investigated parameter ranges, indicating that the nonlinear correlation between the geometric parameter group and the offset/core parameter group is also weak.

Therefore, the two parameter groups can be approximately decoupled within the investigated parameter ranges. The linear and nonlinear correlations motivate us to develop the proposed Dual-Architecture Artificial Neural Network, which can maintain acceptable prediction accuracy while significantly reducing the FEM-labeled data requirement.

III. Methodology of DACouplerNet

This section aims to overcome the reliance on exhaustive data sampling and labeling in modeling traditional IPT magnetic couplers, by leveraging the physical information that the effects of geometric parameters and offset/core parameters can be approximately decoupled, as demonstrated in Section II. The framework of DACouplerNet is proposed in Fig. 7. The definition, data collection, and training of the proposed DACouplerNet are detailed. The workflow of the proposed methodology of DACouplerNet is illustrated in Fig. 8.

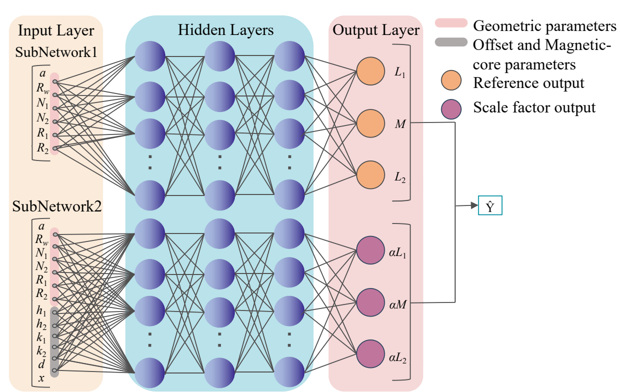

Fig. 7. Framework of the proposed DACouplerNet.

A. Definition of DACouplerNet

The proposed DACouplerNet comprises two subnetworks with different modeling targets, as illustrated in Fig. 7. SubNetwork1 learns the mapping from geometric parameters to the outputs, whereas SubNetwork2 captures the effect of offset and magnetic-core parameters on the same outputs. The final prediction is obtained by aggregating the outputs of these two subnetworks. In this manner, DACouplerNet can accurately predict the mutual inductance and self-inductance of IPT magnetic couplers while reducing the data-sampling overhead.

For SubNetwork1, the inputs include the coil geometry and winding parameters, and the outputs are the coil self- and mutual inductances. Specifically, the input vector $\mathbf{U}_1$ comprises a, R_w, N_1, N_2, R_1, and R_2, while the output vector $\mathbf{Y}_1$ comprises L_1, M, and L_2. This relationship is given by

$$\begin{cases} \mathbf{U}_1 = [a, R_w, N_1, N_2, R_1, R_2], \text{ and} \\ \mathbf{Y}_1 = [L_1, M, L_2]. \end{cases} \tag{8}$$

For SubNetwork2, the inputs include the coil geometry and winding parameters as well as the offset/core parameters. The outputs are the self- and mutual-inductance ratios with respect to a baseline state. Specifically, the input vector $\mathbf{U}_2$ comprises a, R_w, N_1, N_2, R_1, R_2, h_1, h_2, k_1, k_2, d, and x. Although the dominant offset/core-induced inductance variations can be approximately decoupled from the geometric parameters, the geometric inputs are still retained in SubNetwork2 to capture the residual geometry dependence of the normalized inductance ratios. The output vector $\mathbf{Y}_2$ consists of α_{L_1} (the primary self-inductance ratio relative to the baseline), α_M (the mutual-inductance ratio relative to the baseline), and α_{L_2} (the secondary self-inductance ratio relative to the baseline). This relationship is given by

$$\begin{cases} \mathbf{U}_2 = [a, R_w, N_1, N_2, R_1, R_2, h_1, h_2, k_1, k_2, d, x], \text{ and} \\ \mathbf{Y}_2 = [\alpha L_1, \alpha M, \alpha L_2]. \end{cases} \tag{9}$$

The baseline state is defined by $d = 20$ mm, $x = 0$ mm, $k_1 = k_2 = 1$, and $h_1 = h_2 = 2$ mm.

B. Sampling of DACouplerNet

We independently constructed two datasets for DACouplerNet. For SubNetwork1, baseline measurements were collected for all coil dimensional parameters and their corresponding outputs, yielding 11,664 samples. For SubNetwork2, ten representative baseline coils were selected. A coverage-oriented constrained random sampling strategy was used for this selection. Specifically, the geometric parameters (i.e., wire diameter, winding spacing, numbers of primary and secondary turns, and inner diameters of the primary and secondary coils) were sampled within the ranges listed in Table II. During the selection process, the baseline coils were chosen to cover different levels of each geometric parameter as broadly as possible. This strategy enables SubNetwork2 to learn the effects of positional offsets and magnetic-core parameters on the inductance ratios from geometrically diverse coil configurations, rather than from a localized region of the design space.

Finite-element simulations were then performed to generate spatial samples under prescribed step variations in core parameters and positional offsets, thereby establishing a database of self- and mutual-inductance ratios, with 5,184 data points for each baseline coil. For cases with asymmetric primary and secondary parameters, a data augmentation strategy is introduced. By swapping the primary- and secondary-side

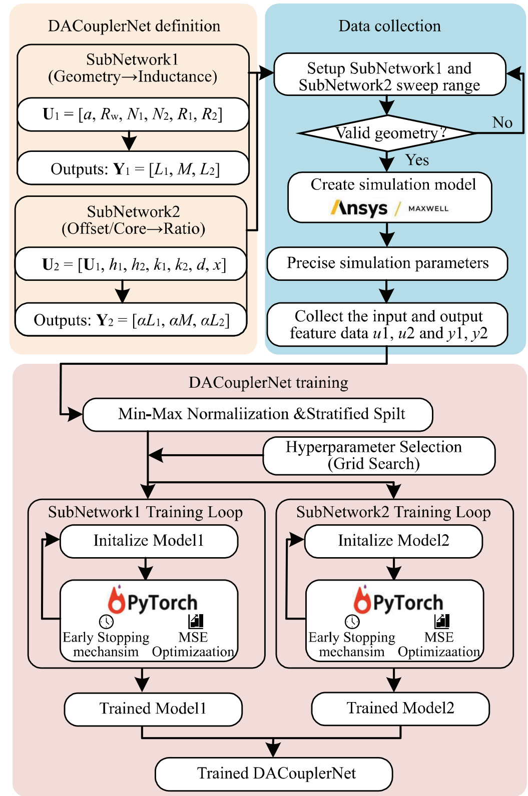

Fig. 8. Workflow of the proposed DACouplerNet.

parameters, additional ratio samples are generated, effectively doubling the dataset size for SubNetwork2.

The input parameters and their ranges are summarized in Table II. In total, $11{,}664 + 10 \times 5{,}184 = 72{,}144$ samples were obtained via finite-element analysis. With the proposed augmentation strategy, the dataset size was further increased to approximately 140,000 samples, which is only about 0.2% of the full investigated parameter-combination space (approximately 7.0×10^7 possible sets).

TABLE II
INPUT PARAMETERS FOR SUBNETWORK1 AND SUBNETWORK2

SubNetwork1 Input Parameters				
Parameter	Definition	Range	Step	Samples
a	Wire diameter	1.6, 2.2, 2.5	–	3
R_w	Winding spacing	0.1–1.1	0.5	3
N_1	Primary winding turns	10–20	2	6
N_2	Secondary winding turns	10–20	2	6
R_1	Primary inner diameter	15–25	2	6
R_2	Secondary inner diameter	15–25	2	6

SubNetwork2 Input Parameters				
Parameter	Definition	Range	Step	Samples
a, N_1, N_2, R_1, R_2, R_w (10 sets)				
h_1	Primary core thickness	1–3	1	3
h_2	Secondary core thickness	1–3	1	3
k_1	Primary core-to-coil outer diameter ratio	0.5–2	0.5	4
k_2	Secondary core-to-coil outer diameter ratio	0.5–2	0.5	4
d	Axial distance	10–60	10	6
x	Lateral distance	0–25	5	6

C. Training of DACouplerNet

To facilitate model training, all input and output variables in both SubNetwork1 and SubNetwork2 are preprocessed using Min–Max normalization to the range of $[0, 1]$, defined as

$$X_{\mathrm{norm}} = \frac{X - X_{\min}}{X_{\max} - X_{\min}}, \tag{10}$$

where X, X_{norm}, $X_{\min}$, and $X_{\max}$ denote the raw value, normalized value, minimum value, and maximum value of the corresponding variable, respectively. For the six input variables shared by the two subnetworks, a common set of normalization parameters is adopted to ensure consistent scaling and avoid mismatch in the representation of the same physical quantity.

The dataset is divided into training and validation subsets using stratified sampling with an 8:2 ratio to preserve a consistent data distribution across subsets. Rectified Linear Units (ReLUs) are employed in the hidden layers to introduce nonlinearity, and are given by

$$\mathrm{ReLU}(x) = \max(0, x). \tag{11}$$

Both SubNetwork1 and SubNetwork2 in DACouplerNet share the same architecture, comprising three hidden layers followed by an output layer. The number of neurons in the hidden layers is selected via grid search according to the dimensionality of the input features. The loss function adopts the mean square error (MSE), which is given by

$$\mathcal{L} = \frac{1}{N}\sum_{i=1}^{N}(y_i - \hat{y}_i)^2. \tag{12}$$

The adaptive moment estimation (Adam) optimizer is used to perform adaptive learning-rate updates, with the parameter update rule given by

$$\theta_t = \theta_{t-1} - \eta \cdot \frac{\hat{m}_t}{\sqrt{\hat{v}_t} + \epsilon}, \tag{13}$$

where $\hat{m}_t$ and $\hat{v}_t$ denote the bias-corrected first- and second-moment estimates, respectively.

Given the larger dataset size of SubNetwork2, a differentiated hyperparameter configuration is adopted. All key hyperparameters are optimized via grid search, resulting in the following settings:

- Batch size: 64 for SubNetwork2 and 32 for SubNetwork1.
- Training epochs: 200 for SubNetwork2 and 180 for SubNetwork1.
- Initial learning rate: selected via a learning-rate sweep, set to 0.03 for SubNetwork2 and 0.003 for SubNetwork1.

The scanning ranges and the corresponding optimal settings of the main hyperparameters for SubNetwork1 and SubNetwork2 are summarized in Table III.

To mitigate overfitting, early stopping is applied. Specifically, training is terminated if the validation loss does not improve for 10 consecutive epochs, and the model parameters corresponding to the minimum validation loss are retained.

A summary of the network architectures and hyperparameter configurations for SubNetwork1 and SubNetwork2 is provided in Table IV.

IV. Experimental verification

This section systematically validates the proposed DACouplerNet from five aspects: comparison with conventional single-architecture ANNs and other dual-architecture regression models, influence of the number of representative baseline coils, data-sampling overhead, and experimental validation on four circular-coupler configurations.

A. Experimental setup

The test dataset is generated using Latin hypercube sampling (LHS), which provides uniform coverage of the parameter space while reducing sample redundancy. A Python-based script with IronPython modules in ANSYS Maxwell is used to perform high-fidelity FEM simulations and calculate the inductances. Compared with conventional random sampling, LHS reduces sample clustering and enables efficient exploration of the high-dimensional parameter space with limited samples.

Four standard regression metrics are adopted to evaluate the prediction accuracy: mean absolute error (MAE), mean absolute percentage error (MAPE), root mean squared error (RMSE), and the coefficient of determination (R^2). Lower MAE, MAPE, and RMSE and higher R^2 indicate better prediction performance.

B. Comparison Between the Proposed DACouplerNet and the Single ANN Model

To isolate the impact of network architecture from data effects and ensure a fair comparison, the sampling density was not increased for either model, and both architectures were trained and tested using exactly the same sampled data points and data-partitioning strategy. Moreover, the hyperparameters of the single ANN were tuned via grid search, so that any performance differences can be more reliably attributed to the architecture design rather than to the choice of hyperparameters.

As shown in Fig. 9, the proposed dual-architecture network exhibits clear advantages over a conventional single-architecture ANN in predicting the target variables L and M. Compared with the conventional ANN (Fig. 9(a)), DACouplerNet (Fig. 9(b)) yields predictions that are more tightly clustered around the diagonal corresponding to the ground-truth values, indicating reduced prediction errors.

The quantitative results further support this observation. As reported in Fig. 9, for L prediction, DACouplerNet achieves an RMSE of 1.1422, corresponding to a 69.95% reduction compared with 3.8005 for the conventional ANN, while R^2 improves from 0.9414 to 0.9979. For M prediction, the MAPE decreases from 23.53% to 4.99%. Overall, the proposed method attains an average prediction error of 4.99% for mutual inductance and 3.05% for self-inductance.

These results demonstrate that DACouplerNet substantially outperforms the conventional ANN architecture.

TABLE III
HYPERPARAMETER SCANNING RANGES AND OPTIMAL SETTINGS OF DACOUPLERNET

SubNetwork1		
Hyperparameter	Scanning Range	Optimal Value
Learning rate	0.001, 0.002, 0.003, 0.004, 0.005, 0.01, 0.02, 0.03	**0.003**
Number of hidden layers	2, 3, 4, 5	**3**
Batch size	16, 32, 64, 128	**32**
Training epochs	100, 120, 140, 160, 180, 200	**180**

SubNetwork2		
Hyperparameter	Scanning Range	Optimal Value
Learning rate	0.001, 0.005, 0.01, 0.02, 0.03, 0.04, 0.05	**0.03**
Number of hidden layers	2, 3, 4, 5	**3**
Batch size	16, 32, 64, 128	**64**
Training epochs	100, 150, 200, 250, 300, 350	**200**

TABLE IV
HYPERPARAMETERS AND NETWORK ARCHITECTURES OF SUBNETWORK1 AND SUBNETWORK2

Parameter	SubNetwork1	SubNetwork2
Input Dimension	6	12
Output Dimension	3	3
Network Architecture	Linear Layer: 6→128 Linear Layer: 128→256 Linear Layer: 256→128 Linear Layer: 128→3	Linear Layer: 12→128 Linear Layer: 128→256 Linear Layer: 256→128 Linear Layer: 128→3
Activation Function	ReLU	ReLU
Loss Function	MSELoss	MSELoss
Optimizer	Adam	Adam
Learning Rate	0.003	0.03
Batch Size	32	64
Training Epochs	180	200

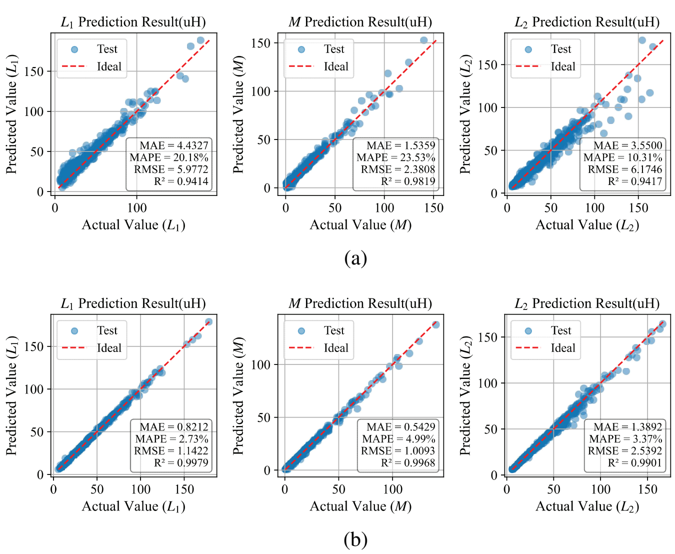

Fig. 9. Comparison between DACouplerNet and single ANN predictions: (a) ANN and (b) DACouplerNet.

C. Comparison Between the Proposed DACouplerNet and the Dual-Architecture Regression Models

In the previous section, DACouplerNet was compared with a conventional single-architecture ANN. To further verify the relative advantages of DACouplerNet within the dual-architecture paradigm, this subsection conducts a horizontal comparison against several dual-architecture regression models.

Specifically, three dual-architecture variants are constructed by extending classical regressors to the same decomposed-learning framework: dual-architecture decision tree (DA-DT), dual-architecture random forest (DA-RF), and dual-architecture gradient-boosted decision tree (DA-XGBoost). In addition, to evaluate the necessity of retaining geometric inputs in SubNetwork2, an ablation model, denoted as DACouplerNet-w/o-GI, is constructed by removing the geometric inputs from SubNetwork2.

It should be noted that the two parameter groups in DACouplerNet are considered approximately decoupled rather than fully independent. SubNetwork1 learns the geometry-dependent baseline inductance values, whereas SubNetwork2 learns the normalized inductance variations caused by the offset and ferrite-core parameters under a given coupler geometry. Although couplers with different geometric dimensions show similar normalized variation trends, these trends are not exactly identical. Therefore, the geometric parameters a, R_w, N_1, N_2, R_1, and R_2 are retained as inputs to SubNetwork2 to capture the residual geometry-dependent effects.

Following the experimental protocol in Section IV-B, all models are trained and evaluated on exactly the same training and test sets, and their hyperparameters are optimized via grid search. The corresponding quantitative results are summarized in Table V.

Table V shows that DACouplerNet consistently achieves the best performance across all evaluation metrics. For the primary self-inductance L_1, DACouplerNet attains the lowest MAE of 0.8212, which is 48.9% lower than the second-best DA-XGBoost (1.6066), and reduces RMSE to 1.1422. For the mutual inductance M, the MAE of DACouplerNet is 0.5429, and the RMSE of 1.0093 is 55.9% lower than that of DA-RF. In terms of R^2, DACouplerNet achieves values above 0.990 for all targets. These results demonstrate the superiority of DACouplerNet for circular-coupler parameter prediction and further validate the effectiveness of the proposed dual-architecture formulation and subnetwork design.

The ablation results further confirm the necessity of retaining the geometric inputs in SubNetwork2. As shown in Table V, removing these geometric inputs leads to larger prediction errors. Specifically, the MAPE values of DACouplerNet-w/o-GI are 4.64%, 10.07%, and 5.12% for L_1, M, and L_2, respectively, whereas the corresponding MAPE values of the complete DACouplerNet are 2.73%, 4.99%, and 3.37%. These results indicate that the offset/core-induced inductance ratios still have weak dependence on the geometric parameters. Therefore, retaining the geometric inputs in SubNetwork2 is necessary to compensate for the residual coupling under the approximate-decoupling assumption.

TABLE V
COMPARISON OF DACOUPLERNET AND DUAL-ARCHITECTURE REGRESSION MODELS

Model	Indicator	Output Parameter		
		L_1	M	L_2
DA-DT	MAE	3.4171	1.8891	3.5370
	MAPE	9.33%	16.61%	9.03%
	RMSE	4.8883	3.0496	5.5314
	R^2	0.9590	0.9704	0.9532
DA-RF	MAE	1.9530	1.1029	2.1837
	MAPE	5.57%	7.65%	5.27%
	RMSE	3.0060	2.2955	4.1174
	R^2	0.9852	0.9832	0.9741
DA-XGBoost	MAE	1.6066	1.2984	1.5802
	MAPE	4.00%	10.73%	3.79%
	RMSE	2.5681	2.5493	2.8371
	R^2	0.9892	0.9793	0.9877
DACouplerNet-w/o-GI	MAE	1.8034	1.1237	2.3010
	MAPE	4.64%	10.07%	5.12%
	RMSE	2.8154	2.1400	4.3164
	R^2	0.9870	0.9854	0.9715
DACouplerNet	MAE	**0.8212**↓	**0.5429**↓	**1.3892**↓
	MAPE	**2.73%**↓	**4.99%**↓	**3.37%**↓
	RMSE	**1.1422**↓	**1.0093**↓	**2.5392**↓
	R^2	**0.9979**↑	**0.9968**↑	**0.9901**↑

D. Influence of the Number of Representative Baseline Coils

As described in Section III-B, SubNetwork2 is trained using samples generated from ten representative baseline coils. To evaluate whether this selection is sufficient, SubNetwork2 is retrained using 2, 4, 6, 8, and 10 representative baseline coils, respectively. For each case, the baseline coils are selected using the same coverage-oriented constrained random sampling strategy, and the same test dataset and evaluation metrics are used for comparison.

The results are shown in Fig. 10. As the number of baseline coils increases, the MAPE values of L_1, M, and L_2 decrease noticeably, indicating that geometrically diverse baseline coils help SubNetwork2 learn more representative offset/core-induced inductance-ratio variations. However, the improvement gradually diminishes when the number approaches ten. Therefore, using ten representative baseline coils provides a reasonable trade-off between prediction accuracy and FEM-labeled data requirement, and the model performance does not rely on the incidental selection of a small number of baseline coils.

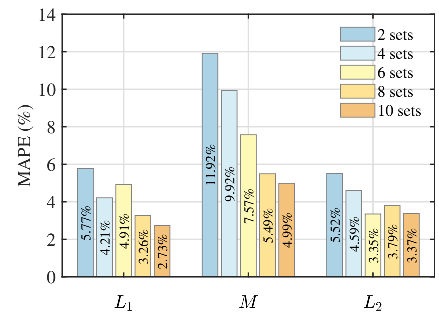

Fig. 10. Comparison of the MAPE of SubNetwork2 using different numbers of representative baseline coils.

E. Reduction of Data-Sampling Overhead

To evaluate the data-sampling overhead, DACouplerNet is compared with representative methods from the literature, as summarized in Table VI. In this comparison, the *full investigated parameter-combination space* denotes all discrete design points considered in each study, the *FEM-labeled samples* denote the samples with FEM-generated labels, and the *training samples* denote the FEM-labeled samples used for model training. The indicator *Samples for training over the full investigated space* is defined as the ratio between the number of training samples and the full investigated parameter-combination space.

As shown in Table VI, the compared methods use 70%–90% of their investigated spaces for training, whereas DACouplerNet uses approximately 1.4×10^5 training samples from a much larger full investigated parameter-combination space of approximately 7×10^7, corresponding to only 0.2%. Therefore, this comparison does not indicate that DACouplerNet always uses fewer training samples in absolute number. Instead, it shows that DACouplerNet can maintain acceptable prediction accuracy with a much lower sampling coverage over a significantly larger design space.

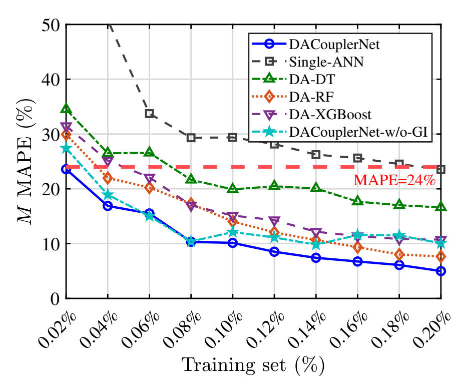

Fig. 11. Sample-efficiency comparison among the six models in terms of the MAPE for mutual-inductance prediction under different values of samples for training over the full investigated space.

To further evaluate the sample efficiency, six models are compared by varying the samples for training over the full investigated space, as shown in Fig. 11. The compared models include DACouplerNet, Single-ANN, DA-DT, DA-RF, DA-

TABLE VI
COMPARISON OF DATA-SAMPLING OVERHEAD BETWEEN DACOUPLERNET AND EXISTING METHODS

Indicator	[20]	[21]	[22]	[23]	DACouplerNet
Input variables	5	6	10	10	12
Full investigated parameter-combination space	27720	4563	1536	5705	∼7e7
FEM-labeled samples	27720	4563	1536	5705	∼1.4e5
Training samples	22176	4107	1075	3994	∼1.4e5
Samples for training over the full investigated space	**80%**	**90%**	**70%**	**70%**	**0.2%**
MAE	–	0.318	–	–	0.9178
MAPE	3.45%	–	–	7.95%	3.7%
R^2	–	–	0.9995	–	0.9949

XGBoost, and DACouplerNet-w/o-GI, and all models are evaluated using the same test dataset and experimental settings.

The results show that DACouplerNet achieves the lowest MAPE for M across all investigated settings. Taking $\mathrm{MAPE} = 24\%$ as a reference accuracy level, DACouplerNet reaches this accuracy with only 0.02% of the full investigated parameter-combination space, whereas the Single-ANN requires approximately 0.20%. Therefore, DACouplerNet reduces the required training samples by about 90% compared with the Single-ANN, corresponding to an approximately tenfold improvement in sample efficiency. The comparisons with DA-DT, DA-RF, DA-XGBoost, and DACouplerNet-w/o-GI further confirm the effectiveness of the proposed dual-architecture design and the retention of geometric inputs in SubNetwork2.

F. Experimental Verification

In Sections IV-B and IV-C, DACouplerNet demonstrated significant advantages in the experimental comparisons. However, to ensure its reliability in practical applications, it is necessary to validate the model predictions through physical measurements.

This subsection describes a dedicated experimental platform designed to directly assess DACouplerNet's ability to predict real coupler parameters.

As shown in Fig. 12, the platform comprises a moving stage, a transmitting coil, a receiving coil, and an impedance analyzer (HIOKI IM3536 LCR meter). The moving stage is fabricated from ABS, whose permeability is close to that of air, thereby minimizing disturbances to the magnetic-field distribution. Using this stage, both the axial distance d and the lateral offset x can be precisely adjusted.

Both the self- and mutual-inductance measurements were performed at 85 kHz. Under each test condition, three consecutive measurements were taken after the LCR meter readings had stabilized, and their average was used as the final measured value.

Four coupler prototypes (Coil-A, Coil-B, Coil-C, and Coil-D) are designed according to the parameters listed in Table VII. The structural parameters are precisely controlled using 3D-printed coil fixtures, and the resulting coil prototypes are shown in Fig. 13.

The coils are wound with multi-strand litz wire to effectively minimize the skin effect at high frequencies, with tin-plated terminals. The ferrite material used is TDK PC95, which has a relative permeability of $\mu_r = 3300$.

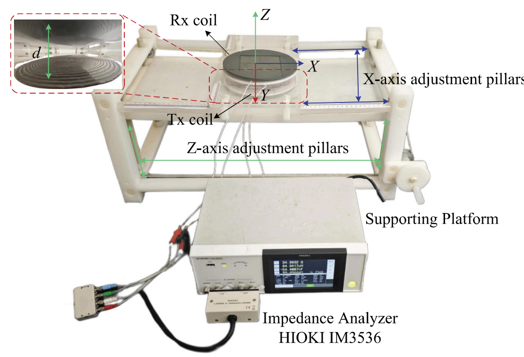

Fig. 12. Experimental prototype.

TABLE VII
PARAMETERS OF DIFFERENT SOLENOID COIL CONFIGURATIONS

Solution	a/mm	R_w/mm	N_1	N_2	R_1/mm	R_2/mm	h_1/mm	h_2/mm	k_1	k_2
Coil-A	2.5	0.6	17	14	23	19	2	2	1	1
Coil-B	1.6	1.1	20	20	19	19	3	3	1	1
Coil-C	2.2	0.1	18	16	23	25	3	2	1	2
Coil-D	2.2	1.1	20	20	25	25	3	3	1	1

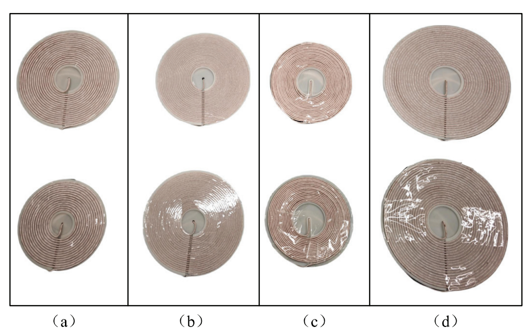

Fig. 13. Coupler demos: (a) Coil-A, (b) Coil-B, (c) Coil-C, and (d) Coil-D.

The experimental verification consists of two stages as follows.

1) Alignment Condition Verification: The transmitting and receiving coils were precisely aligned with an axial distance of $d = 30$ mm and a lateral offset of $x = 0$ mm.

First, the self-inductance and mutual inductance of all coils were measured under the aligned condition at $d = 30$ mm. The

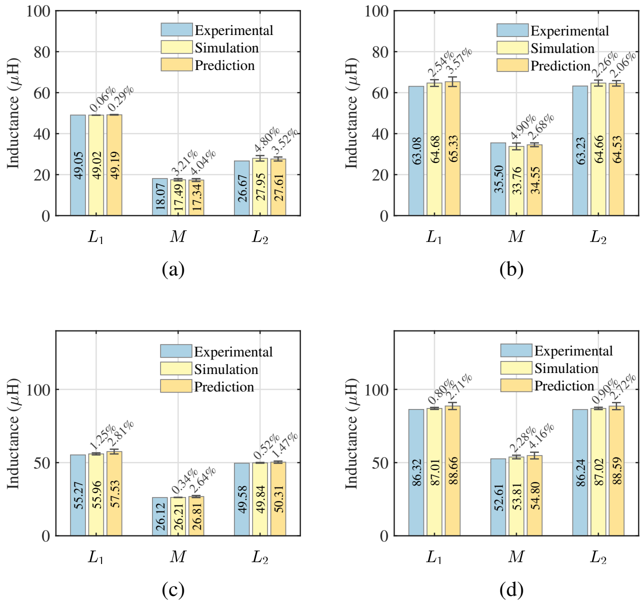

Fig. 14. Comparison of self-inductance and mutual inductance predicted values, simulation values and experimental values of different prototype coils: (a) Coil-A, (b) Coil-B, (c) Coil-C, and (d) Coil-D.

relative errors among the experimental measurements, finite-element simulation results, and the proposed DACouplerNet predictions are compared in Fig. 14. For all prototype coils, DACouplerNet yields self- and mutual-inductance predictions with only small relative errors with respect to the experimental results. Moreover, the error trends of DACouplerNet closely follow those obtained from the FEM simulations.

2) Offset Condition Verification: Under offset conditions, M is affected more significantly than L_1. Although L_1 may exhibit small variations due to core-induced eddy-current effects, its absolute change is much smaller than that of M. Motivated by this observation, this subsection evaluates the prediction accuracy for mutual inductance under transverse and longitudinal offsets, using Coil-A and Coil-B as representative cases.

For the lateral offset experiment, the axial distance was fixed at $d = 30$ mm, while the lateral offset x was increased from 0 to 25 mm in 5 mm increments. At each offset position, the mutual inductance M was measured and recorded. The measured results were then compared with finite-element simulations and DACouplerNet predictions. The detailed results are summarized in Fig. 15. In this experiment, d is fixed at 30 mm, and $x \in 0, 5, 10, 15, 20, 25$ mm; the comparison includes experimental measurements, FEM results, and DACouplerNet predictions at each offset.

For the axial offset experiment, the lateral offset x was fixed at 0 mm, while the axial spacing d was incrementally increased from 10 mm to 60 mm in steps of 10 mm. At each position, M was measured, and its attenuation trend with increasing d was recorded. The experimental results are presented in Fig. 16.

The experimental results prove that under different lateral offsets and different axial distances, this method effectively

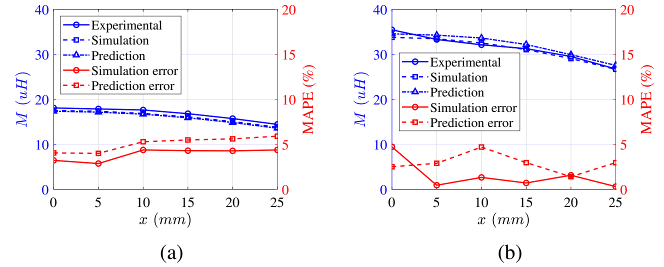

Fig. 15. Comparison of the predicted mutual inductance values, simulation values and experimental values of Coil-A and Coil-B under different lateral offsets: (a) Coil-A, and (b) Coil-B.

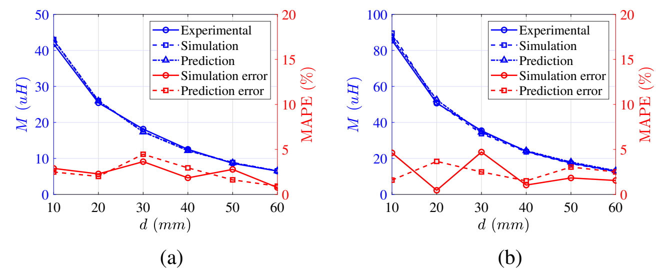

Fig. 16. Comparison of the predicted mutual inductance values, simulation values and experimental values of Coil-A and Coil-B under different axial distances: (a) Coil-A, and (b) Coil-B.

captures the variation law of physical parameters, and the error of the predicted value relative to the experimental value is always controlled within 6%.

V. Conclusion

In this paper, we identify that the effects of geometric parameters and offset/core parameters on mutual inductance and self-inductance can be approximately decoupled within the investigated parameter ranges. Leveraging this insight, we propose DACouplerNet, a dual-architecture artificial neural network for IPT magnetic-coupler modeling with reduced FEM-labeled data requirement. DACouplerNet substantially improves the prediction accuracy of both self-inductance and mutual inductance across coils with varying dimensions, core configurations, and offset conditions. Moreover, it significantly reduces the requirement for labeled training data, achieving effective training with samples for training accounting for only 0.2% of the full investigated parameter-combination space. Experimental results based on circular magnetic couplers show that the mutual-inductance prediction error is reduced from 23.53% for the conventional single-ANN model to 4.99%, demonstrating its effectiveness for circular-coupler design optimization. Although the model construction and experimental validation in this work are mainly based on circular magnetic couplers, the proposed dual-architecture modeling framework is not inherently restricted to circular coils. For other unipolar and bipolar coil designs, the framework can be extended by defining topology-specific geometric variables and re-verifying the approximate-decoupling assumption between the parameter groups. Overall, the proposed approach provides an efficient and cost-effective tool for IPT magnetic coupler modeling.

References

[1] G. A. Covic and J. T. Boys, "Inductive power transfer," *Proc. IEEE,* vol. 101, no. 6, pp. 1276–1289, Jun. 2013.

[2] A. Mahesh, B. Chokkalingam, and L. Mihet-Popa, "Inductive wireless power transfer charging for electric vehicles–A review," *IEEE Access,* vol. 9, pp. 137667–137713, 2021.

[3] D. Patil, M. K. McDonough, J. M. Miller, B. Fahimi, and P. T. Balsara, "Wireless power transfer for vehicular applications: Overview and challenges," *IEEE Trans. Transport. Electrific.,* vol. 4, no. 1, pp. 3–37, Mar. 2018.

[4] B. Zou and Z. Huang, "Primary-frequency-tuning and secondary-impedance-matching IPT converter with programmable constant power output and optimal efficiency tracking against variation of coupling coefficient," *IEEE Trans. Power Electron.,* vol. 39, no. 4, pp. 4895–4909, Apr. 2024.

[5] C. Liu, C. Jiang, J. Song, and K. T. Chau, "An effective sandwiched wireless power transfer system for charging implantable cardiac pacemaker," *IEEE Trans. Ind. Electron.,* vol. 66, no. 5, pp. 4108–4117, May 2019.

[6] Y. Zhang, S. Chen, X. Li, and Y. Tang, "Design methodology of free-positioning nonoverlapping wireless charging for consumer electronics based on antiparallel windings," *IEEE Trans. Ind. Electron.,* vol. 69, no. 1, pp. 825–834, Jan. 2022.

[7] C. R. Teeneti, T. T. Truscott, D. N. Beal, and Z. Pantic, "Review of wireless charging systems for autonomous underwater vehicles," *IEEE J. Oceanic Eng.,* vol. 46, no. 1, pp. 68–87, Jan. 2021.

[8] F. Lu, H. Zhang, H. Hofmann, W. Su, and C. C. Mi, "A dual-coupled LCC-compensated IPT system with a compact magnetic coupler," *IEEE Trans. Power Electron.,* vol. 33, no. 7, pp. 6391–6402, Jul. 2018.

[9] C. Zhang, Y. Yao, and Y. Wang, "Decoupling optimization of the three-coil coupler for IPT system featuring high efficiency and misalignment tolerance," *IEEE Trans. Ind. Electron.,* vol. 70, no. 9, pp. 8918–8927, Sep. 2023.

[10] G. Rituraj and P. Kumar, "A new magnetic structure of unipolar rectangular coils in WPT systems to minimize the ferrite volume while maintaining maximum coupling," *IEEE Trans. Circuits Syst. II, Exp. Briefs,* vol. 68, no. 6, pp. 2072–2076, Jun. 2021.

[11] H. Altun and N. Pirinçi, "A novel analytical model for mutual inductance calculations between two nonidentical N-sided polygonal planar coils arbitrarily positioned in 3-D space for wireless power transfer," *IEEE Trans. Power Electron.,* vol. 38, no. 8, pp. 10396–10411, Aug. 2023.

[12] W. G. Hurley and M. C. Duffy, "Calculation of self- and mutual impedances in planar sandwich inductors," *IEEE Trans. Magn.,* vol. 33, no. 3, pp. 2282–2290, May 1997.

[13] S. Liu, J. Su, J. Lai, J. Zhang, and H. Xu, "Precise modeling of mutual inductance for planar spiral coils in wireless power transfer and its application," *IEEE Trans. Power Electron.,* vol. 36, no. 9, pp. 9876–9885, Sep. 2021.

[14] M. Lu and K. D. T. Ngo, "Analytical calculation of proximity-effect resistance for planar coil with litz wire and ferrite plate in inductive power transfer," *IEEE Trans. Ind. Appl.,* vol. 55, no. 3, pp. 2984–2991, May-June 2019.

[15] M. Wu, X. Wei, G. A. Covic, and J. T. Boys, "Modeling of litz-wire DD coil with ferrite core for wireless power transfer system," *IEEE Trans. Power Electron.,* vol. 38, no. 5, pp. 6653–6669, May 2023.

[16] S. Raju, R. Wu, M. Chan, and C. P. Yue, "Modeling of mutual coupling between planar inductors in wireless power applications," *IEEE Trans. Power Electron.,* vol. 29, no. 1, pp. 481–490, Jan. 2014.

[17] R. Qin, J. Li, and D. Costinett, "A 6.6-kW high-frequency wireless power transfer system for electric vehicle charging using multilayer nonuniform self-resonant coil at MHz," *IEEE Trans. Power Electron.,* vol. 37, no. 4, pp. 4842–4856, Apr. 2022.

[20] M. Kim, M. Jeong, M. Cardone, and J. Choi, "Design of a spiral coil for high-frequency wireless power transfer systems using machine learning," *IEEE J. Emerg. Sel. Topics Ind. Electron.,* vol. 5, no. 1, pp. 193–202, Jan. 2024.

[18] R. Bosshard and J. W. Kolar, "Multi-objective optimization of 50 kW/85 kHz IPT system for public transport," *IEEE J. Emerg. Sel. Topics Power Electron.,* vol. 4, no. 4, pp. 1370–1382, Dec. 2016.

[19] Z. Luo, X. Wei, M. G. S. Pearce, and G. A. Covic, "Multiobjective optimization of inductive power transfer double-D pads for electric vehicles," *IEEE Trans. Power Electron.,* vol. 36, no. 5, pp. 5135–5146, May 2021.

[21] W. Ding, Y. Wang, T. Chen, Z. Lu, Y. You, J. Wang, and Z. Huang, "A stacking machine-learning based method for accelerating magnetic coupler design with ferrite cores in inductive power transfer applications," *Int. J. Circ. Theor. Appl.,* vol. 1, no. 14, pp. 1–14, May 2024.

[22] J. Liu, X. Xie, S. Yang, C. Zhu, X. Zhang, and F. Lu, "A general data-driven design methodology of magnetic couplers for wireless power transfer systems," *IECON 2022 – 48th Annu. Conf. IEEE Ind. Electron. Soc.,* Brussels, Belgium, 2022, pp. 1–6.

[23] X. Du and D. Dujic, "Modeling and design optimization of loosely coupled PCB spiral coils in inductive power transfer systems," *IEEE Trans. Power Electron.,* vol. 38, no. 11, pp. 13430–13442, Nov. 2023.

[24] Y. Wu, J. Zhang, K. T. Chau, and C. Liu, "Precise coil inductance prediction in WPT systems: A transfer learning approach," *IEEE Trans. Transport. Electrific.,* vol. 11, no. 2, pp. 7083–7095, Apr. 2025.

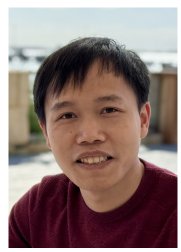

Zhicong Huang (Senior Member, IEEE) received the B.Eng. degree in electrical engineering and automation and the M.Eng. degree in mechanical and electronic engineering from Huazhong University of Science and Technology, Wuhan, China, in 2010 and 2013, respectively, and the Ph.D. degree in power electronics from The Hong Kong Polytechnic University, Hong Kong, China, in 2018.

Since 2020, he has been an Associate Professor with Shien-Ming Wu School of Intelligent Engineering, South China University of Technology, Guangzhou, China. His research interests include wireless power transfer, resonant power conversion, large-scale renewable power generation, artificial intelligence for power electronics, and wave energy converters.

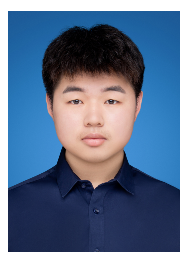

Jun Cheng received the B.E. degree in mechanical engineering from Chongqing Jiaotong University, Chongqing, China, in 2023. In 2026, he received the M.S. degree in electronic information engineering from South China University of Technology, Guangzhou, China, where he is pursuing the Ph.D degree in control science and engineering. His current research interest is wireless power transfer.

Guozhen Hu was born in Hubei Province,China, in 1979. He received Ph.D. from Huazhong University of Science and Technology, Wuhan, China in 2012. He worked as a Postdoc in Wuhan University from 2016 to 2018. He is currently a full professor in HuBei Polytechnic University, Huangshi, China. His current research interests include modeling and control of power electronic converter, wireless power transmission of contactless power supply system.